Coupled effect of microstructure and topology on the mechanical behavior of Inconel718 additively manufactured lattices

S. Banait [a], C. Liu [b], M. Campos [c], M.S. Pham [b], M.T. Pérez-Prado [a],*

[a] Imdea Materials Institute, Calle Eric Kandel, 2, 28906 Getafe, Madrid, Spain
[b] Engineering Alloys, Dept. of Materials, Imperial College London, London, UK
[c] Dept. Materials Science and Engineering, IAAB, Universidad Carlos III de Madrid (UC3M), Av. De la Universidad 30, 28911 Leganés, Spain

HIGHLIGHTS

- The microstructure of as-built Inconel718 lattices is formed by randomly oriented fine equiaxed grains populated with cell boundaries containing Nb.
- Precipitation leads to a transition in the mechanical behavior of Inconel718 FCC, FCCXYZ, and HCP lattices from bending-dominated to stretch-dominated.
- Precipitation leads to a transition in the strut deformation mode from plastic hinging to elastic buckling.
- The variations of lattice strength can be related to that of the base material in similar microstructure and testing conditions.

GRAPHICAL ABSTRACT
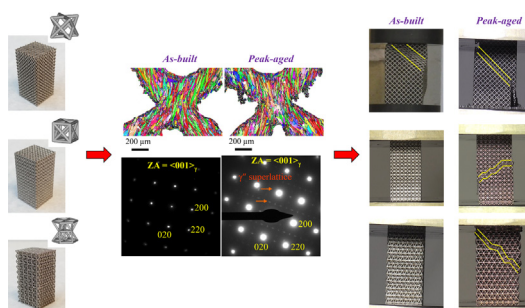
ARTICLE INFO

ABSTRACT

LPBF-manufactured Inconel718 lattices with six cubic and hexagonal structures and with two material microstructures (as-built, without γ" precipitation, and heat-treated, with γ" precipitates, but with similar cell/grain size, shape and texture) were compressed at room temperature and at 600 °C. The behavior of the base material under identical microstructure and test conditions was also investigated using dedicated LPBF-manufactured specimens with single strut gauges. Irrespective of topology, precipitation led to a transition in the lattice mechanical behavior from bending-dominated to stretch-dominated, which was associated to a change in the strut deformation mode from plastic hinging to elastic buckling, as well as to a decrease in the base material strain to fracture. For all topologies investigated, precipitation led to lattice strengthening, consistent with particle-strengthening of the base material. Additionally, high temperature straining resulted both in a decrease in the lattice yield strength, consistent with softening of the base material, and in a reduction in the width of the stress oscillations in the stretch-dominated lattices, which is associated to the decrease in the base material ductility. This work proves that material microstructure influences strongly the behavior of additively manufactured architectured structures and that it must be considered as a design criterion for performance optimization.

© 2022 The Author(s). Published by Elsevier Ltd. This is an open access article under the CC BY license (http://creativecommons.org/licenses/by/4.0/).

* Corresponding author.
  E-mail address: teresa.perez.prado@imdea.org (M.T. Pérez-Prado).

1. Introduction

Periodic strut-based lattices are 3D-constructed by the repetition of unit cells of different structures, including body centred cubic (BCC), face centred cubic (FCC), and hexagonal-closed packed (HCP), among many others [1]. With outstanding specific mechanical properties, they are regarded as excellent candidates for structural applications in transport as they provide an opportunity to reduce material waste and to limit emissions without compromising performance [2]. Moreover, these complex metamaterials are endowed with tunable stiffness, a key property for biodegradable bone implants, and with outstanding thermal conductivity, which is a well sought requirement for heat exchangers [3].

The advent of additive manufacturing (AM) has widely expanded the design space for metallic lattices [4,5]. In particular, LPBF, a process in which a laser source consolidates consecutive layers of metallic powders following a pre-defined path, has proven to be a robust method to fabricate lattices with extremely complex geometries and high reproducibility [1]. Furthermore, this method ensures a relatively good surface quality and reduced material internal porosity, both of which are especially critical when the structure is formed by very fine struts. Progress in LPBF process optimization has allowed to fabricate lattices with strut dimensions close 200 μm, although minimum feature sizes are a function of the material and printing system [6].

Strut-based lattices exhibit mainly-two types of behavior when subjected to a compressive load [1,3,6,7]. In some lattices, following a first stage of elastic deformation, the stress remains constant until relatively large plastic strains, beyond which densification starts. This type of mechanical response is observed in lattice structures of "bending-dominated" struts, and it is in general preferred for applications in energy absorption components due to its high predictability. In other lattices the elastic regime is followed by sudden stress bursts associated with the periodic concentration of strain along planar shear bands. This behavior is termed "stretch-dominated". Such lattices are less preferred for energy absorption applications because shear band formation, which is dependent of the lattice type and loading directions [8], precludes a proper prediction of their performance.

It has been well established that lattice topology has a governing influence on the mechanical behavior of lattices [9,9–18] and several models have been put forward to relate architecture and mechanical performance with the aim of improving the predictability and of optimizing the lattice design. For example, the Maxwell criterion, based on the Maxwell number ($M = s-3n + 6$, where s is the number of struts, and n is the number of nodes) [1,7,19], states that topologies with $M < 0$ are bending-dominated, whereas those with $M \geq 0$ are stretch-dominated. This model predicts that typical strut-based lattices, including BCC, BCCZ, FCC, FCCZ, and diamond architectures, among others, are bending-dominated [3,10]. Experimental data, however, do not always comply with these predictions. For example, Leary et al. [10] reported a stretch-dominated response in Inconel 625 BCCZ and FCCZ lattices. Similarly, Yu et al. [11] observed a stretch-dominated response in AlSi10Mg microlattices with a diamond structure ($M = -14$). On the other hand, the Gibson-Ashby model [20] predicts that the ratios of the mechanical properties (elastic modulus, yield strength) of a given lattice with respect to those of the constituent base material are proportional to the lattice relative density. However, systematic attempts to rationalize all the existing evidence within the frame of this model, such as that carried out by Maconachie *et al.* [1], also yielded a relatively small correlation between experimental observations and model predictions for several lattice architectures. All this evidence suggests that, besides topology, the properties of the base metallic material, which in metallic alloys are highly dictated by its microstructure, might have a critical influence on the mechanical behavior of lattices. A handful of studies have analyzed the influence of annealing following LPBF processing on the mechanical behavior of lattices [21–25]. However, in these works the isolated effect of individual microstructural parameters were not thoroughly explored. Moreover, the coupled effect of architecture and individual microstructural features in LPBF processed strut-based lattices is still widely unexplored.

The aim of this work is to analyze the isolated influence of precipitation in Inconel718 additively manufactured lattices with multiple architectures at room and high temperatures. With that purpose, LPBF of several cubic and hexagonal strut-based lattices were printed and tested at room temperature and at 600 °C at quasi-static rates. Post-LPBF aging heat treatments were carefully optimized to induce controlled precipitation without altering other microstructural parameters. The mechanical behavior of the peak-aged lattices thus developed was also measured under similar testing conditions and compared to that of the as-built lattices. The coupled effect of precipitation and topology was analyzed in order to establish a basis for the design of lattices with improved structural performance.

2. Materials and methods

2.1. Experimental work

The feedstock material utilized for this work was gas atomized Inconel718 powder purchased from Oerlikon. The composition of the powder is summarized in Table 1. Fig. 1a illustrates the monomodal particle size distribution and the corresponding d_{10}, d_{50}, and d_{90} values, which amounted, respectively, to 25, 40, and 63 μm. The apparent density, tapped density and flowability values of the powder, which were measured using a standard Hall apparatus, are, respectively, 4.5 g/cm^3, 4.9 g/cm^3, and 15 s. Fig. 1b confirms that the morphology of the powders ranges from spherical to ellipsoidal and that most particles contain satellites.

Six strut-based lattices with external dimensions of approximately 20x20x40 mm^3, and with FCC and HCP topologies, were printed by LPBF in a Renishaw AM400 system furnished with a reduced build volume (RBV) platform. In all cases, the build direction (BD) was parallel to the long axis of the lattice. Fig. 2 illustrates the as-built LPBF lattices after support removal: FCC (Fig. 2a), FCCXYZ, i.e., FCC with additional struts parallel to the X, Y and Z directions (Fig. 2b), HCP with the c-axis parallel to BD (HCP0, Fig. 2c), HCP with the c-axis perpendicular to BD (HCP90, Fig. 2d), HCP with the c-axis at 45° with respect to BD and with open ends (HCP45, Fig. 2e), and HCP with the c-axis at 45° with respect to BD and with an outer frame boundary (HCP45B, Fig. 2f). Lattice structures were designed using nTopology. In all cases, the strut diameter was 0.4 mm. The cubic lattices were manufactured with 2.5 × 2.5 × 2.5 mm^3 unit cells. In the HCP lattices, a = 2.5 mm and the c/a ratio was chosen to be equivalent to that of a typical HCP alloy such as pure magnesium (1.624), where the most compact plane is the basal plane. The relative densities of the six lattices investigated (ρ/ρ_s, where ρ_s is the density of bulk Inconel718, amounting to 8.2 g/cm^3) are the following: FCC (0.15), FCCXYZ (0.2), HCP0 (0.14), HCP90 (0.14), HCP45 (0.13), and HCP45B (0.15). LPBF manufacturing was carried out using a bidirectional scanning strategy with a layer thickness of 30 μm and with 67° rotation between two consecutive layers. The processing parameters, which were optimized to obtain high consolidation using a Design of Experiments (DoE) strategy, were P (laser power) = 100 W, v (scan speed) = 875 mm/s (exposure time = 50 μs

Table 1
Chemical composition of the Inconel718 powder (wt.%).

Ni	Cr	Co	Al	Nb	Ti	Fe
49.5–50	18.7–19	0.066–0.070	0.38–0.4	4.6–4.8	0.45–0.5	13.5–13.8
Mo	**Mn**	**Si**	**Cu**	**Ta**	**P**	**Zr**
1.6–1.65	0.054–0.057	0.35–0.39	0.23–0.25	<0.01	<0.01	<0.005
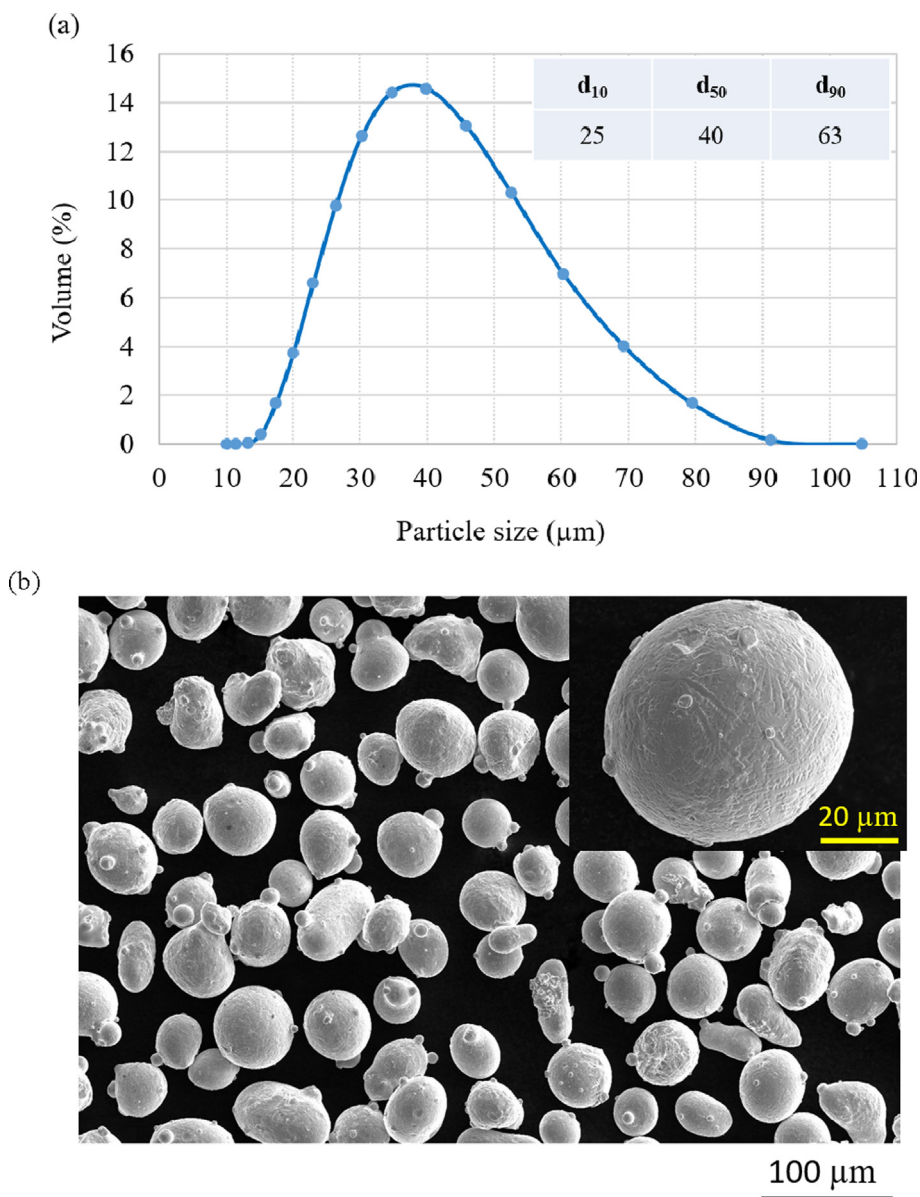
Fig. 1. (a) Particle size distribution of the feedstock Inconel 718 powders, including d_{10}, d_{50} and d_{90} values (in μm); (b) SEM micrograph illustrating particle morphology.

and point distance = 70 μm), and h (hatch distance) = 90 μm. Under these conditions, a robust manufacturing campaign could be put in place to print lattices with high geometric accuracy and high reproducibility. The average area fraction of porosity, measured from optical micrographs of cross sections perpendicular to BD using the ImageJ image analysis software, was 0.44 %.

In order to better understand the mechanical behavior of the LPBF-processed lattices, cylindrical dogbone coupons with the gauge's diameter and length identical to those of individual lattice struts (0.4 mm in diameter and 10 mm in length) were manufactured vertically by LPBF using the same set of processing parame-

ters that were utilized to manufacture the lattices. Fig. 3a illustrates the additively manufactured tensile coupons attached to the RBV platform, prior to support removal. The porosity volume fraction in these specimens, measured by X-ray computerised tomography (XCT) using a Phoenix X-ray (General Electric) Nanotom 160NF system. The experimental conditions used to carry out the tomography measurements were 130 kV, 60 μA and a W target with a Cu filter of 0.2 mm. The resolution achieved was of 6 μm/pixel. Fig. 3b is a 3D image reconstruction of the gauge length of one tensile specimen, illustrating the internal porosity distribution. The measurement gave the porosity of 0.21 ± 0.1 %. Although
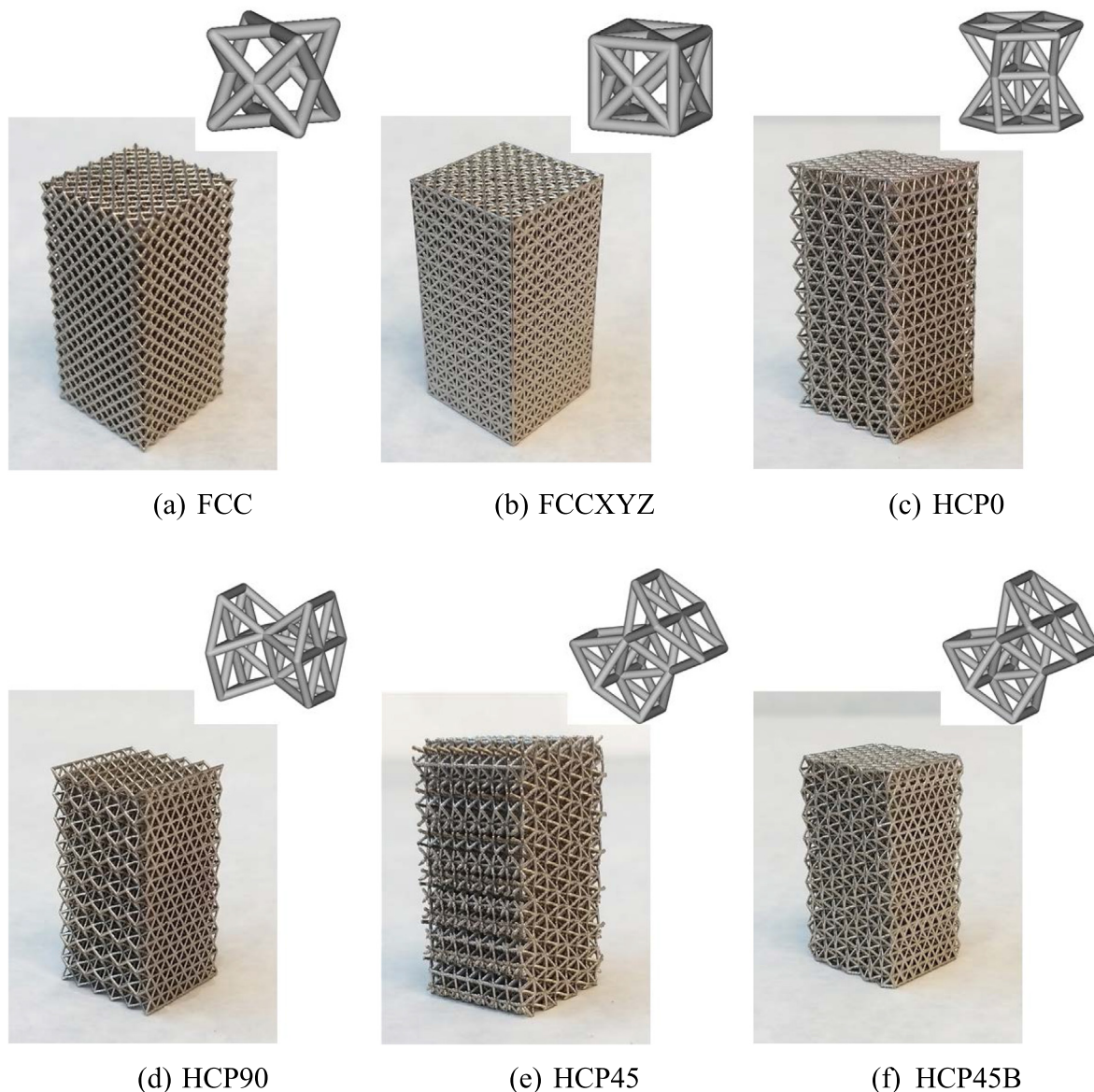
Fig. 2. 3D printed lattices, with six different topologies. (a) FCC; (b) FCCXYZ; (c) HCP with the c-axis parallel to the vertical direction (HCP0); (d) HCP with the c-axis parallel to the horizontal direction (HCP90); (e) HCP with the c-axis at 45° with respect to the vertical direction and with open ends (HCP45); (f) HCP with the c-axis at 45° with respect to the vertical direction and with an outer boundary (HCP45B).

XCT is different to the optical microscopy used to quantify the porosity in the lattice struts, the higher density of pores measured for the lattice struts was expected as the quality of lattice struts should be lower than that of vertically built dogbone strut specimens because of over-hanging issues often encountered for multi-orientated struts. The lower quality of lattice struts raised a need of recalibration on the material property parameters for simulation (described in the Sections 2.2 and 4.2).

Following LPBF manufacturing selected lattices were subjected to an aging heat treatment study at 718 °C by introducing them in a muffle furnace for increasing periods of time followed by air cooling to room temperature. The mentioned aging temperature was chosen because it is commonly used in standard Inconel718 aging treatments [26–28]. Fig. 4 illustrates the evolution of the Vickers hardness with aging time. The hardness was measured in polished cross sections of the as-built and aged lattices perpendicular to the BD using a Shimadzu microhardness indenter, with forces of 4.9 and 9.8 N, respectively, and a dwelling time of 15 s.

Ten hardness measurements were performed for each condition. The hardness of the as-built lattices (317 ± 8 HV) increased during aging up to a maximum of 502 ± 9 HV after 6 h. It must be noted that the measured hardness levels achieved following the direct aging treatment, and in the absence of any solutionizing step, are similar or higher than those reported for peak aged Inconel718 following the standard two-stage heat treatment [29,30], and somewhat lower than those achieved by direct double aging (535 HV) [31,32]. Treatments longer than about 8–10 h resulted in softening of the lattice material. On the light of these findings, several lattices with the six topologies investigated, as well as some single-strut tensile specimens, were heat treated under peak-aging conditions (718 °C, 6 h) in order to understand the effect of aging on the mechanical behavior.

The microstructures of the as-built and peak-aged lattices were examined at different magnifications using several complementary techniques. First, electron backscattered diffraction (EBSD) was used to characterize the grain size, measured by the linear inter-
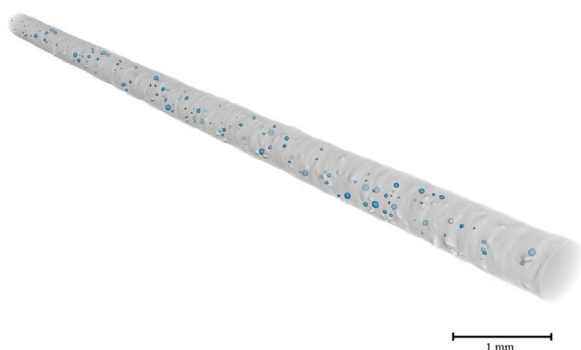
(a)

(b)

1 mm
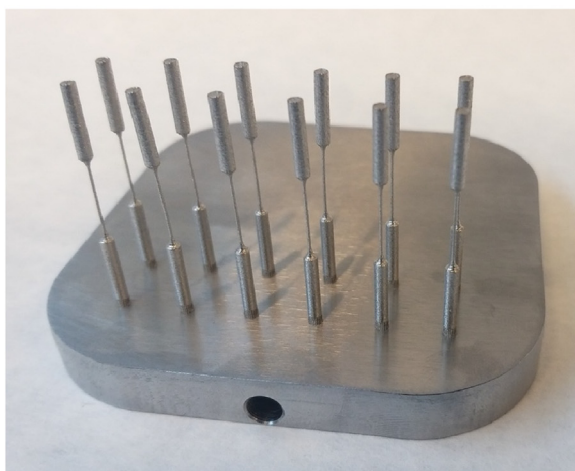
Fig. 3. 3D printed tensile specimens, designed to measure the mechanical behavior of single-struts at room and high temperature. (a) Specimens attached to the build plate, prior to support removal; (b) 3D tomographic reconstruction of the gauge length, where the internal pores have been colored in blue. (For interpretation of the references to color in this figure legend, the reader is referred to the web version of this article.)

Fig. 4. Aging curve illustrating the evolution of the Vickers microhardness following heat treatments at 718 °C up to a cumulative time of 150 h.

cept method, the microtexture, and the grain boundary distribution. EBSD was performed in a focused ion beam field emission gun scanning electron microscope (FIB-FEGSEM, FEI Helios Nano-Lab DualBeam) equipped with an HKL system, a CCD camera, and both the Aztec and the Channel 5.0 data acquisition and analysis software packages. EBSD measuring conditions included a current of 2.7nA, a step size of 1.1 μm, and an accelerating voltage of 30 kV. The as-built and peak-aged microstructures were also examined by transmission electron microscopy (TEM) with a FEI Talos F200x microscope operating at 200 KV. Energy dispersive spectrometry (EDS) was utilized to analyze the composition of segregated species and second phase particles. Sample preparation for TEM consisted on the extraction of electron-transparent thin lamellae from selected regions of the strut interiors by FIB milling, as described in detail in [33].

As-built and peak-aged lattices with each of the six topologies investigated were compressed at room temperature and at 600℃ using an initial crosshead speed of 0.3 mm•min^{-1} in an Instron 3384 universal testing machine. The compression axis was parallel to BD. Tests were observed to be highly reproducible (see Supplementary Fig. 1), which attests to the robustness of the printing pro-
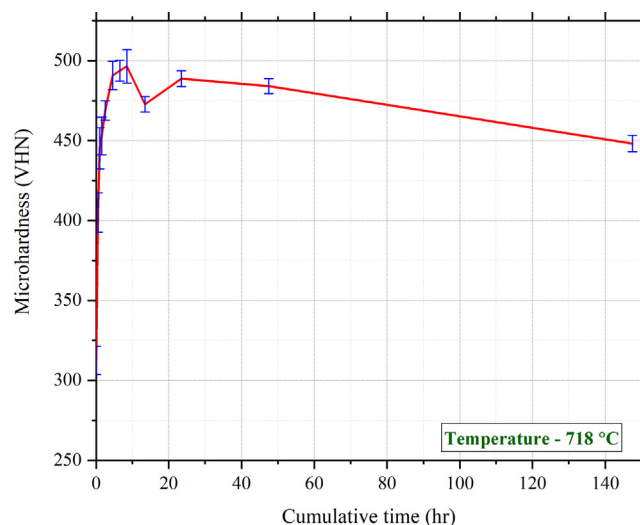
cess. At least two tests were carried out per testing condition. High temperature tests were performed using an Ibertest IB TR331100 climatic chamber. A high-resolution camera (Correlation Solutions Stingray Allied F504B ASG) was used to capture live videos of the compression of the lattices at both room and high temperatures in order to facilitate the investigation of the deformation and fracture mechanisms. Additionally, the tensile behavior of the LPBF processed single-strut tensile coupons was also measured in the as-built and peak-aged conditions, at room temperature and 600℃, and at an initial crosshead speed of 0.3 mm•min^{-1} in order to study the effect of microstructure on the material properties. The strain was estimated from the crosshead displacement.

2.2. Simulation

FEA modeling was carried out using Abaqus/Explicit to simulate the deformation and strain localization during compression of some of the studied lattice structures. Lattice models for FEA were meshed using Timoshenko B31 beam elements with an approximate element length of 1.5 mm. The orientations of beams were assigned parallel to the directions of struts. The material property parameters (such as the elastic modulus and yield strength) for simulations (shown in Table 2) were obtained from the tensile true stress–strain curves of as-built and peak-aged cylindrycal dogbone samples that were fabricated vertically with the gauge diameter of the same size as the lattice strut's diameter as described earlier in Section 2.1. Despite of using the same process parameters as for the lattice struts, the cylindrical samples should contain different grain microstructure because the thermal profile should be different in fabrication of single cylinder in comparison to multi-orientated struts in the lattice structures. In addition, the level of porosity and roughness in the cylinder samples might be also slightly different to the lattice struts due to thermal profile and build orientations (with the lattice struts having more porosity, see Section 2.1). Thus, the mechanical behaviour of the tensile cylindrical samples were expected to be different to the behaviour of single struts in the lattice. Therefore, the obtained values for parameters for the simulation of the lattice structures needed recalibration to produce a good fit against the experimental data of lattice structures. The fitting showed that the value of yield stress obtained from tensile test (Fig. 3) need to be recalibrated. The recalibrated stresses of Inconel718 in as-built and peak-aged con-

Table 2
Mechanical properties of the base material for FEA.

	Density (g/cm^3)	Young's Modulus (GPa)	Poisson's Ratio	Yield strength (MPa)	Ultimate tensile strength (MPa)
As-built	8.2	72	0.284	539	920
Aged	8.2	92	0.284	1357	1615

ditions were given in Table 2. In addition, the values of the apparent elastic modulus for the as-built and peak-aged Inconel718 were adjusted to 72 GPa and 92 GPa, respectively. Such used values of elastic modulus reflected the effect of porosity and surface roughness that degraded the stiffness of the intricate lattice struts.

To simulate the compression, two rigid plates meshed by R3D4 elements with a size of 2 mm were created as compression plates. The bottom plate was fixed with tie constraints applied to the bottom nodes and struts of lattice. The top plate was moving in the direction perpendicular to the plate towards the bottom plate to com-
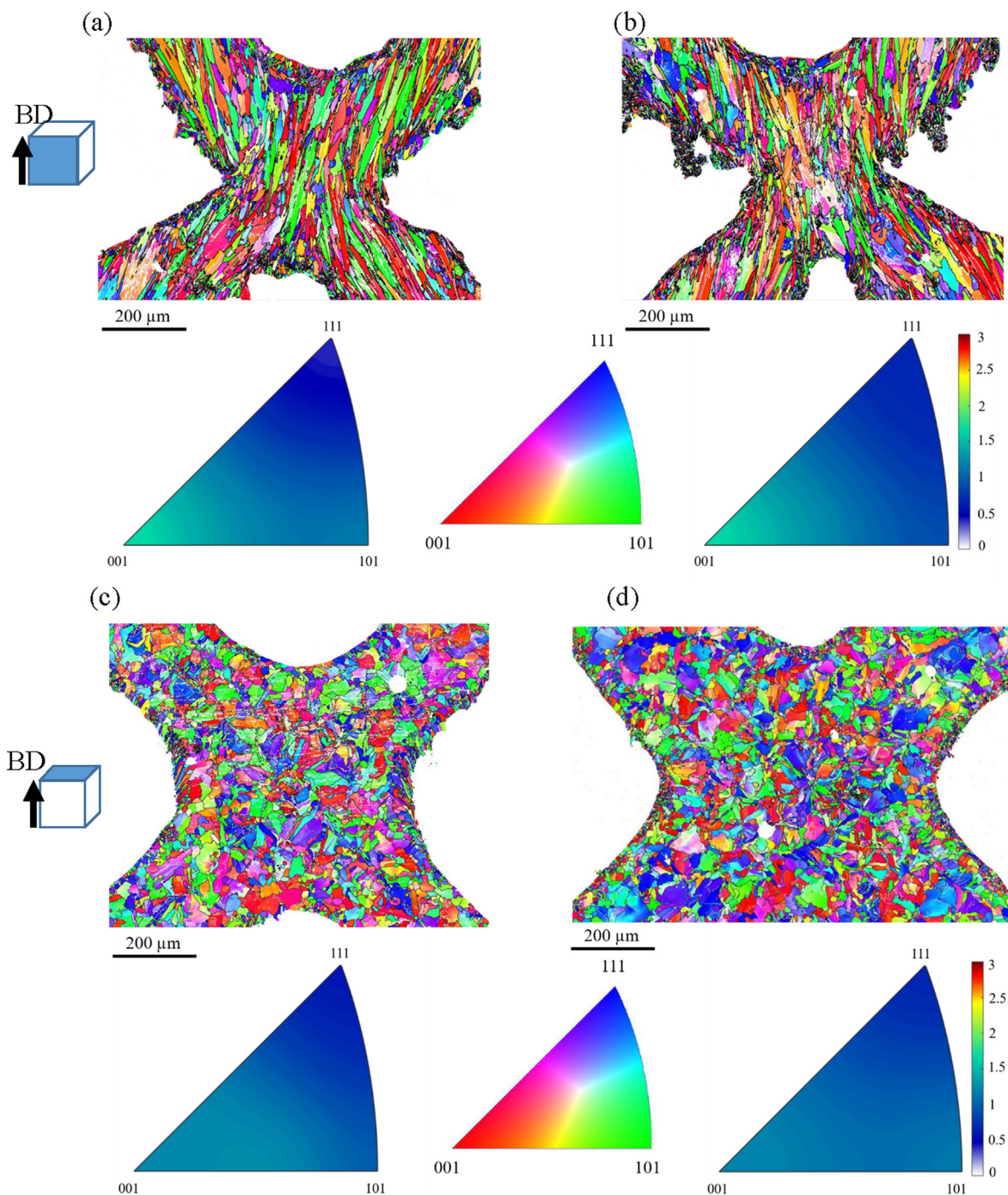

Fig. 5. EBSD inverse pole figure maps (IPF) in the BD illustrating the microstructure and the microtexture of the FCC as-built (a,c) and peak-aged (b,d) lattices. (a,b) Cross-section parallel to BD; (c,d) cross section perpendicular to BD. The insets on the left illustrate the orientation of the examined cross-section with respect to BD. An inverse stereographic triangle illustrating the orientation of the BD has been placed next to each condition. The orientation color coding is also included as an inset.

press the lattice. A general hard contact and a friction coefficient of 0.2 were used for all lattice simulations. To simultaneously ensure the quasi-static simulation and reduce the computing time, the mass of lattice was scaled by a factor of 256 with kinetic energy of lattice controlled less than 1 % of total energy during the compression.
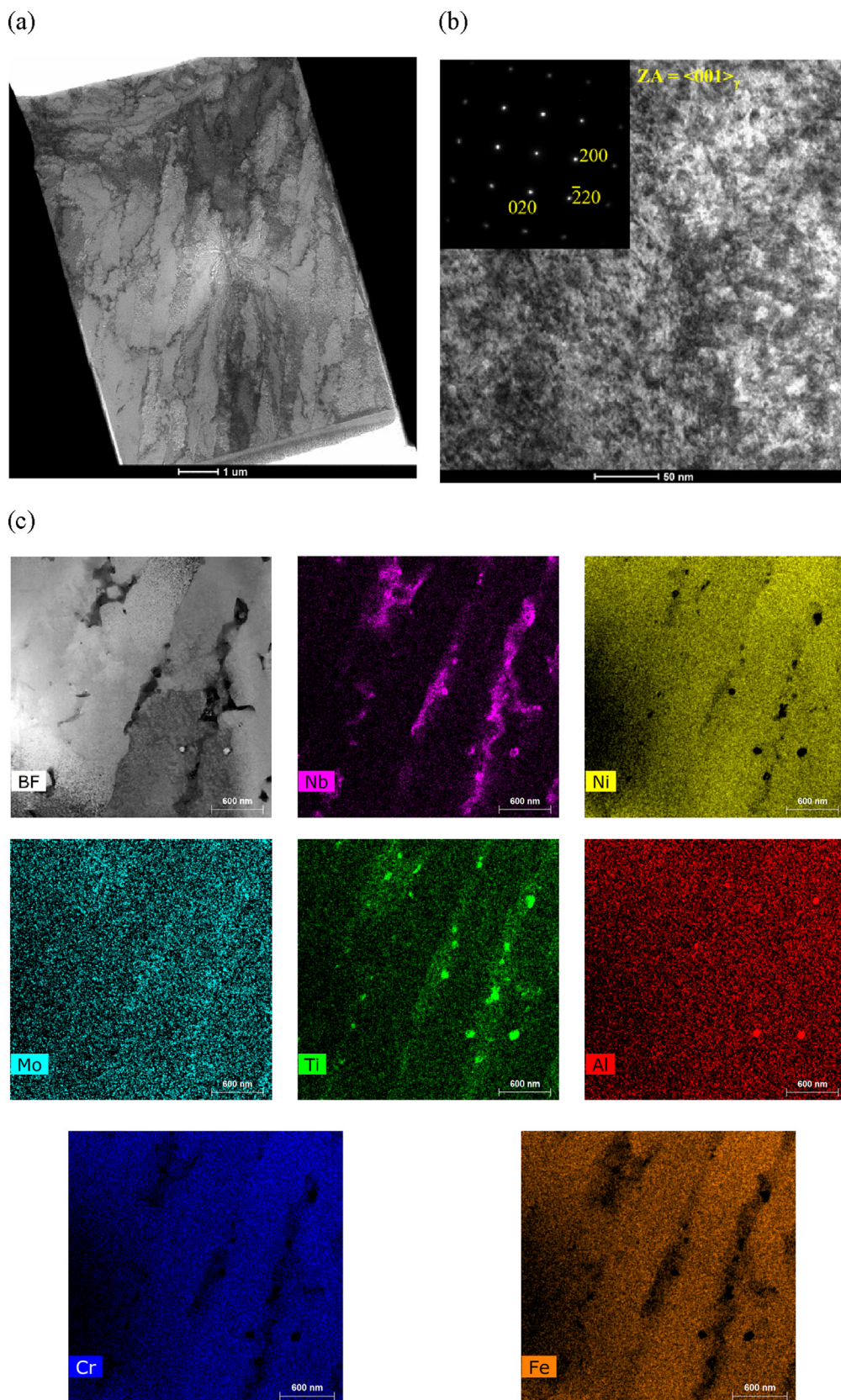
(a)

(b)

(c)

Fig. 6. TEM examination of the as–built FCC lattice along a $\langle 0\,0\,1 \rangle_\gamma$ zone axis. (a) Bright field micrograph illustrating the cellular structure; (b) Bright field micrograph and the corresponding selected area diffraction pattern illustrating the interior of a cell; (c) EDS maps depicting the distribution of different elements in a selected area.
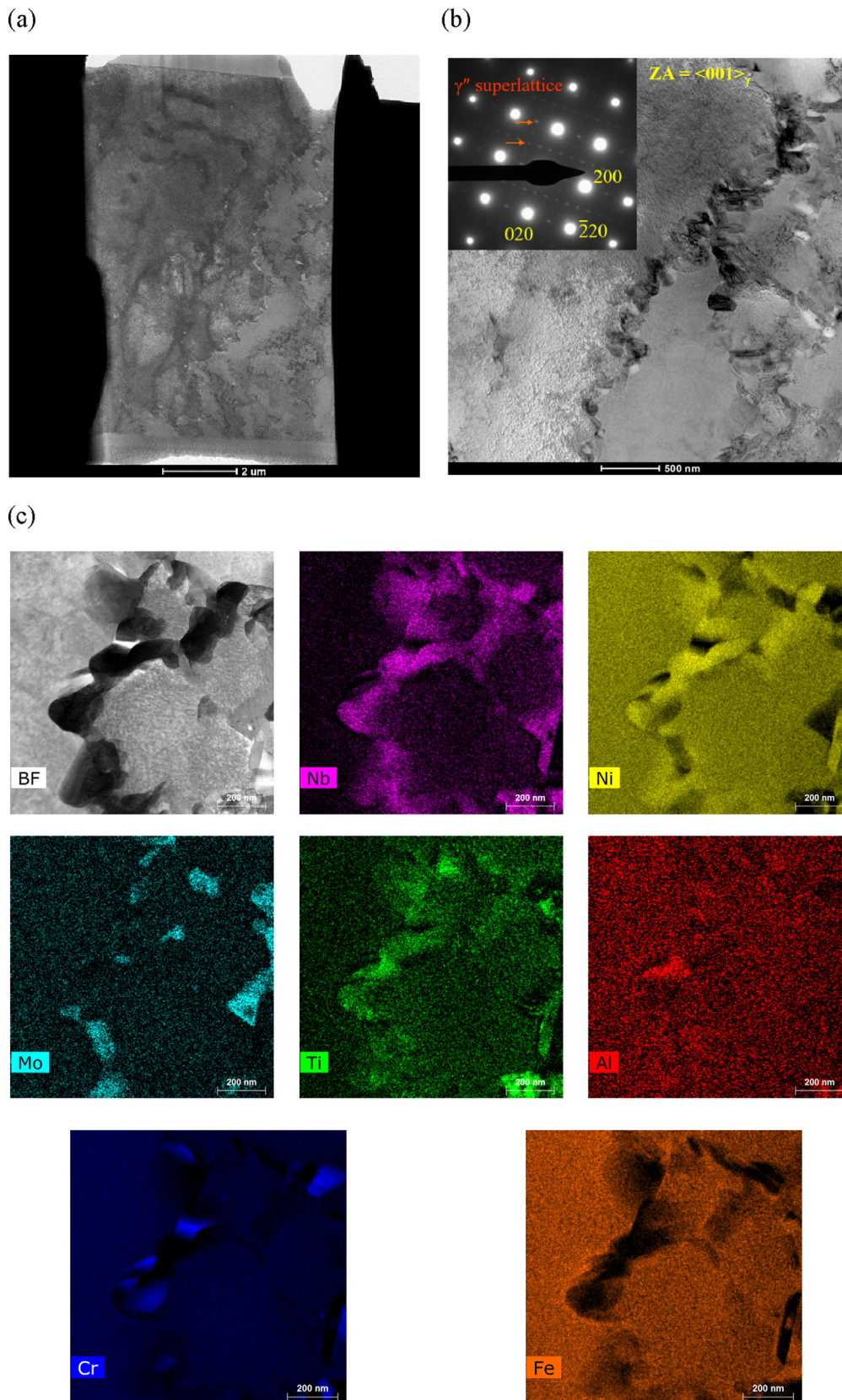
(a)

(b)

(c)

Fig. 7. TEM examination of the heat-treated FCC lattice along a $\langle 0\,0\,1 \rangle_{\gamma}$ zone axis. (a) Bright field micrograph illustrating the cellular structure; (b) Bright field micrograph at higher magnification and the corresponding selected area diffraction pattern. The orange arrows highlight the superlattice spots; (c) EDS maps depicting the distribution of different elements in a selected area. (For interpretation of the references to color in this figure legend, the reader is referred to the web version of this article.)
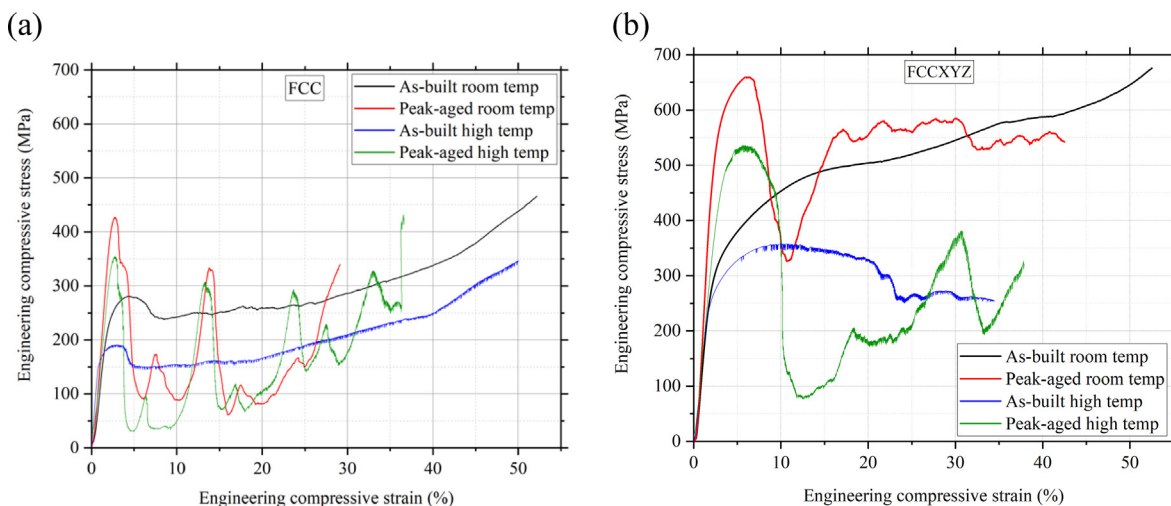
(a)

(b)

Fig. 8. Specific engineering compressive stress–strain curves corresponding to the (a) FCC and (b) FCCXYZ Inconel 718 3D printed lattices tested at room and high (600 °C) temperatures. Data corresponding to the two microstructures investigated (as-built and peak-aged) are shown. Tests were carried out using an initial cross-head speed of 0.3 mm•min^{-1}.

3. Results

3.1. Microstructure of the Inconel718 as-built and peak-aged lattices.

The as-built material microstructure was found to be similar for all lattices, irrespective of their architectures. This is consistent with the fact that a common set of processing parameters was used to print all the lattices and that they all have the same strut dimensions. For the sake of brevity, we will show here only the microstructure of the FCC lattice.

Fig. 5 compares the polycrystalline microstructure and the microtexture of the Inconel718 FCC as-built and peak-aged lattices along cross sections parallel to BD (Fig. 5a and 5b, respectively) and perpendicular to BD (Fig. 5c and 5d, respectively). Several EBSD inverse pole figure maps showing the crystallographic orientations with respect to the BD are included. Fig. 5 reveals that the aging treatment did not lead to any significant changes in the grain size, shape, and orientation. Grains were slightly elongated along BD both in the as-built and peak-aged conditions. The average grain length and width are, respectively, 16 ± 28 μm and 10 ± 14 μm in the as-built lattice, and 13 ± 26 μm and 9 ± 10 μm in the peak-aged lattice. The crystallographic texture is basically random in both conditions, with only a slight tendency for the ⟨001⟩ directions to align with the BD, as indicated in the corresponding inverse stereographic triangles. The aging treatment did not lead to any major changes in the misorientation of the grain boundary network. In both cases, as is typical of LPBF processed superalloys [29–31], a high fraction of low angle boundaries, with misorientations smaller than 5°, was present.

Fig. 6 shows the microstructure of the as-built FCC lattice in more detail. Fig. 6a is a bright field TEM micrograph illustrating the cell structure. The interior of an individual cell, and the corresponding selected area diffraction (SAD) pattern are included in Fig. 6b. It can be seen that cell interiors are supersaturated solid solutions and therefore only one set of diffraction spots, corresponding to the Ni superalloy matrix (γ), is visible in the SAD pattern. Such spots have been labelled using yellow indexes. The gray contrast in Fig. 6b denotes the presence of some solute clusters and some dispersed nanoparticles, which do not give rise to any additional reflections in the corresponding SAD pattern. Fig. 6c is a collection of EDS maps in which it can be seen that segregation, mostly of Nb, takes place at cell boundaries. Following aging

(Fig. 7) the cell size remained similar (Fig. 7a), but precipitation of γ″ particles clearly took place. The presence of such precipitates is evidenced by the appearance of additional reflections in the corresponding SAD pattern (Fig. 7b), which are highlighted using orange arrows. The EDS maps of Fig. 7c reveal Nb, Mo, and Ti segregation at cell boundaries.

In summary, the key difference between the as-built and peak-aged lattices is, thus, the presence of γ″ precipitates in the treated samples, while other microstructural features such as the cell size, the grain size, morphology and orientation, as well as the nature of the grain boundaries, are similar in both conditions.

### 3.2. Influence of precipitation on the mechanical behavior of cubic lattices.

Fig. 8 illustrates the specific (i.e., normalized by the relative density) compressive stress–strain curves corresponding to the as-built and peak-aged lattices with FCC (Fig. 8a) and FCCXYZ (Fig. 8b) topologies. The corresponding room temperature and high temperature (600 °C) mechanical behavior are compared in the same figure and the yield strength values are summarized in Table 3. Several trends can be inferred from Fig. 8. First, the FCC lattice is weaker than the FCCXYZ lattice due to the presence of added ⟨001⟩ struts in the latter. Second, in the as-built condition, both cubic lattices exhibit predominantly a bending dominated

Table 3
Lattice yield strength values corresponding to Inconel718 3D printed lattices at room and high temperature.

Lattice yield strength (MPa)	As-built	Peak-aged
FCC, RT	132	332
FCCXZ, RT	213	365
HCP0, RT	122	450
HCP90, RT	100	250
HCP45, RT	90	220
HCP45B, RT	85	212
FCC, 600 °C	142	265
FCCXZ, 600 °C	116	335
HCP0, 600 °C	100	300
HCP90, 600 °C	55	160
HCP45, 600 °C	84	185
HCP45B, 600 °C	93	180
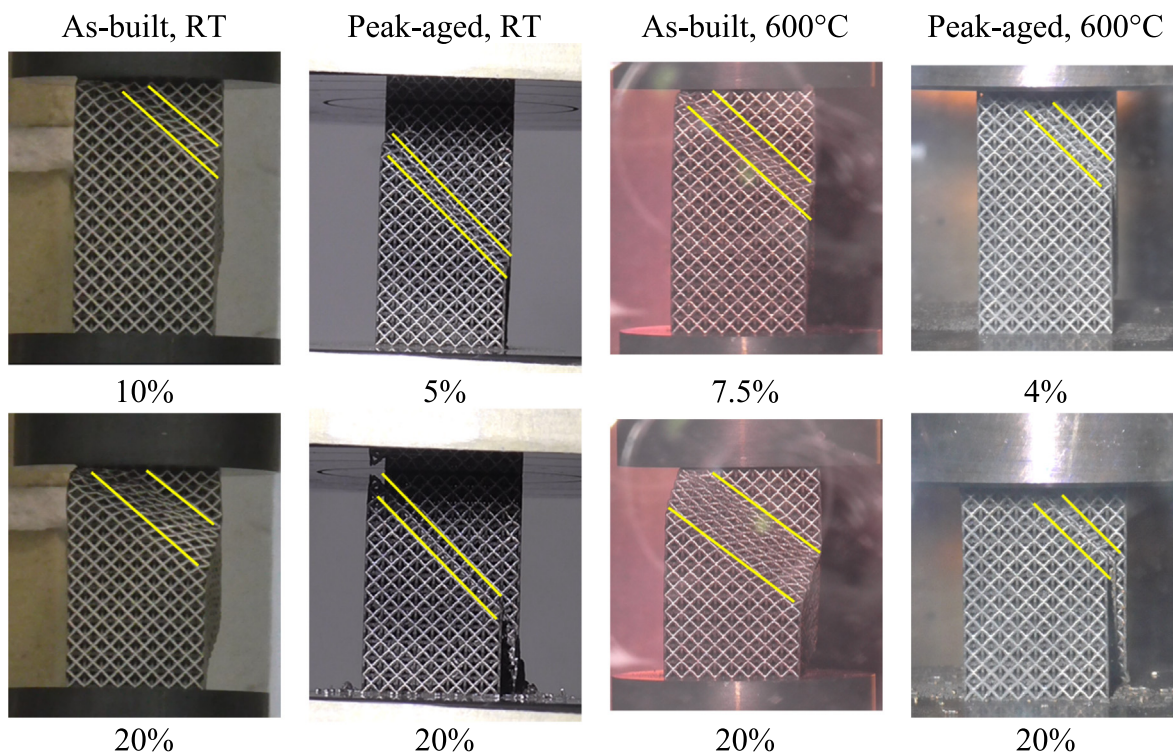
(a) **FCC**
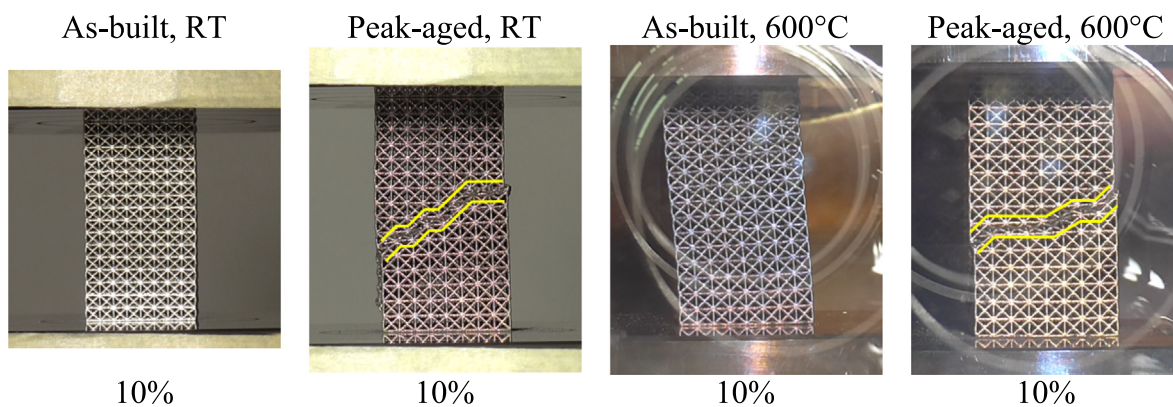
(b) **FCCXYZ**

Fig. 9. Surfaces of the as-built and peak-aged (a) FCC and (b) FCCXYZ lattices at different nominal strain levels. The corresponding engineering strains are indicated below each image.

behavior, in which a stress plateau is clearly apparent following yielding and prior to the densification stage. In the FCC lattice, however, a stress peak, similar to a yield point phenomenon often seen in metals [34], is observed prior to the stress plateau. At the two temperatures investigated, precipitation due to the age treatment leads to strengthening and to a transition to a stretch-dominated behavior. For a given microstructure, increasing the test temperature to 600 °C does not give rise to any change in the deformation mode (bending or stretch-dominated) but it leads to a reduction in the average width of the stress serrations (i.e., the average strain amplitude of the serrations) of the peak-aged lattices (Fig. 8a).

Fig. 9a shows the surfaces of the as-built and peak-aged FCC lattices at different nominal strain levels, both at room and high temperatures. In the as-built condition, at the two temperatures investigated, strain concentrated during the first deformation stages along a band that makes an angle of about 45° with respect to the compression axis. Within the mentioned band, which became wider with increasing strain, struts deformed plastically to a large extent without fracture (i.e. plastic hinges). The stages of band formation and band propagation were associated, respectively, to the stress maximum and to the stress plateau observed following yielding in the curves corresponding to the as-built FCC lattices in Fig. 8a. On the other hand, the peak-aged FCC lat-

tices failed by the break-up of the struts along a plane making an angle of about 45° with respect to the compression axis at the two temperatures investigated, leading to the dramatic stress decrease observed in Fig. 8a at strains close to 0.05. Fig. 10 provides a magnified view of strut plastic deformation (Fig. 10a) and strut failure (Fig. 10b) in as-built and peak-aged lattices, respectively. Supplementary videos 1a and 1b illustrate the room temperature compression of FCC as-built and peak-aged lattices. All observations suggest that little or no plastic deformation occurred before fracture of peak-aged struts.

Fig. 9b illustrates the surfaces of the as-built and peak-aged FCCXYZ lattices at different strain levels, both at room and high temperature. In the as-built condition, irrespective of temperature, homogeneous lattice deformation can be observed at a strain of 10 %. In the peak-aged lattices, at that same strain, premature strut breaking along a band formed by steps that were both perpendicular and at approximately 45° with respect to the compression axis takes place, leading to the dramatic stress decrease observed in Fig. 8b. Due to the presence of the additional struts in FCCXYZ lattice, the path of the shear band consisted of steps perpendicular to the compression axis and at 45° with respect to the compression axis. Supplementary videos 2a and 2b illustrate the room temperature compression of FCCXYZ as-built and peak-aged lattices.

3.3. Influence of precipitation on the mechanical behavior of hexagonal lattices.

Fig. 11 illustrates the specific compressive room and high temperature stress–strain curves corresponding to the as-built and peak-aged lattices with HCP0 (Fig. 11a), HCP90 (Fig. 11b), HCP45 (Fig. 11c,e), and HCP45B (Fig. 11d,f) topologies. The yield stress values are summarized in Table 3. Several trends can be inferred from Fig. 11. First, a distinctive characteristic of the deformation of the HCP90 lattice is the presence of a serration at strains comprised between 0.02 and 0.03 (Fig. 11b), irrespective of microstructure and temperature. Second, for a given temperature, precipitation in both peak-aged HCP0 and HCP90 lattices leads to strengthening and to a transition from a bending-dominated response to a stretch-dominated response. Finally, for a given microstructure, increasing the test temperature results in softening and in a decrease in the width of the stress serrations of the peak-aged lattices, but it does not lead to any change in the deformation mode.

In the HCP45 and HCP45B lattices (Fig. 11c,e and d,f respectively) the mechanical behavior was stretch-dominated irrespective of microstructure, and consecutive stress serrations are observed from the early stages of deformation. The HCP45B lattice

was stronger due to the presence of the outer boundary segments. On average, for a given temperature, precipitation leads to strengthening and to an increase in the stress drop associated to the observed stress serrations. For a given microstructure, increasing the test temperature did not alter the deformation mode but it resulted in moderate softening and in a reduction of the average width of the stress serrations.

Fig. 12 illustrates the surfaces of the as-built and peak-aged HCP0 (Fig. 12a), and HCP90 (Fig. 12b) lattices at different strain levels, both at room and high temperature. In the as-built condition, irrespective of architecture, lattice deformation was seen to proceed by the homogeneous bending of struts, while in the aged lattices precipitation led to strut break-up along stepped bands, which were highlighted in yellow. Additionally, Fig. 12b confirms that a stress serration appearing in the HCP90 lattices following yielding (see black dotted line in Fig. 11b) was not associated to the formation of a shear band, as no such band was visible in the lattices deformed up to strains close to 5 %, which was larger than that at which the serration was observed. The origin of this small stress serration was elucidated with the aid of FEM modeling in the "Discussion" section. Supplementary videos 3a and 3b illustrate the room temperature compression of HCP90 as-built and peak-aged lattices.

Fig. 13 illustrates the surfaces of the as-built and peak-aged HCP45 (Fig. 13a), and HCP45B (Fig. 13b) lattices, compressed at room and high temperature up to a nominal strain of 2 %. In both cases, it can be seen that the structures deformed and failed along bands that make an angle of 45° with respect to the compression axis. Inside these bands, struts in the as-built lattices were plastically deformed, while they were already fractured in the peak-aged lattices. With increasing strain, parallel shear bands encompassing the entire lattice volume develop in both the as-built and peak-aged lattices, irrespective of temperature. Fig. 14 shows, as an example, a HCP45B as-built lattice deformed up to a strain of 30 %. Supplementary videos 4a and 4b illustrate the room temperature compression of HCP45 as-built and peak-aged lattices.

4. Discussion

4.1. Effect of precipitation and test temperature on the properties of the base material.

In order to rationalize the mechanical behavior of the investigated lattices, it is necessary to examine first the influence of microstructure on the mechanical response of the as-built and peak-aged Inconel718 superalloy (base material). Fig. 15 illustrates
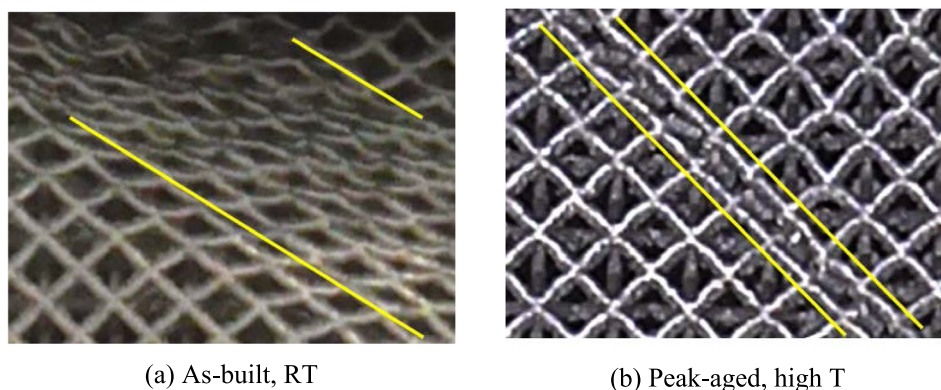

(a) As-built, RT   (b) Peak-aged, high T

Fig. 10. Magnified view of strut deformation and failure as a function of the material microstructure in FCC lattices. (a) Strut plastic deformation during compression an as-built lattice (e = 17 %); (b) strut breakage along localized shear bands during compression of a peak-aged lattice (e = 5 %).
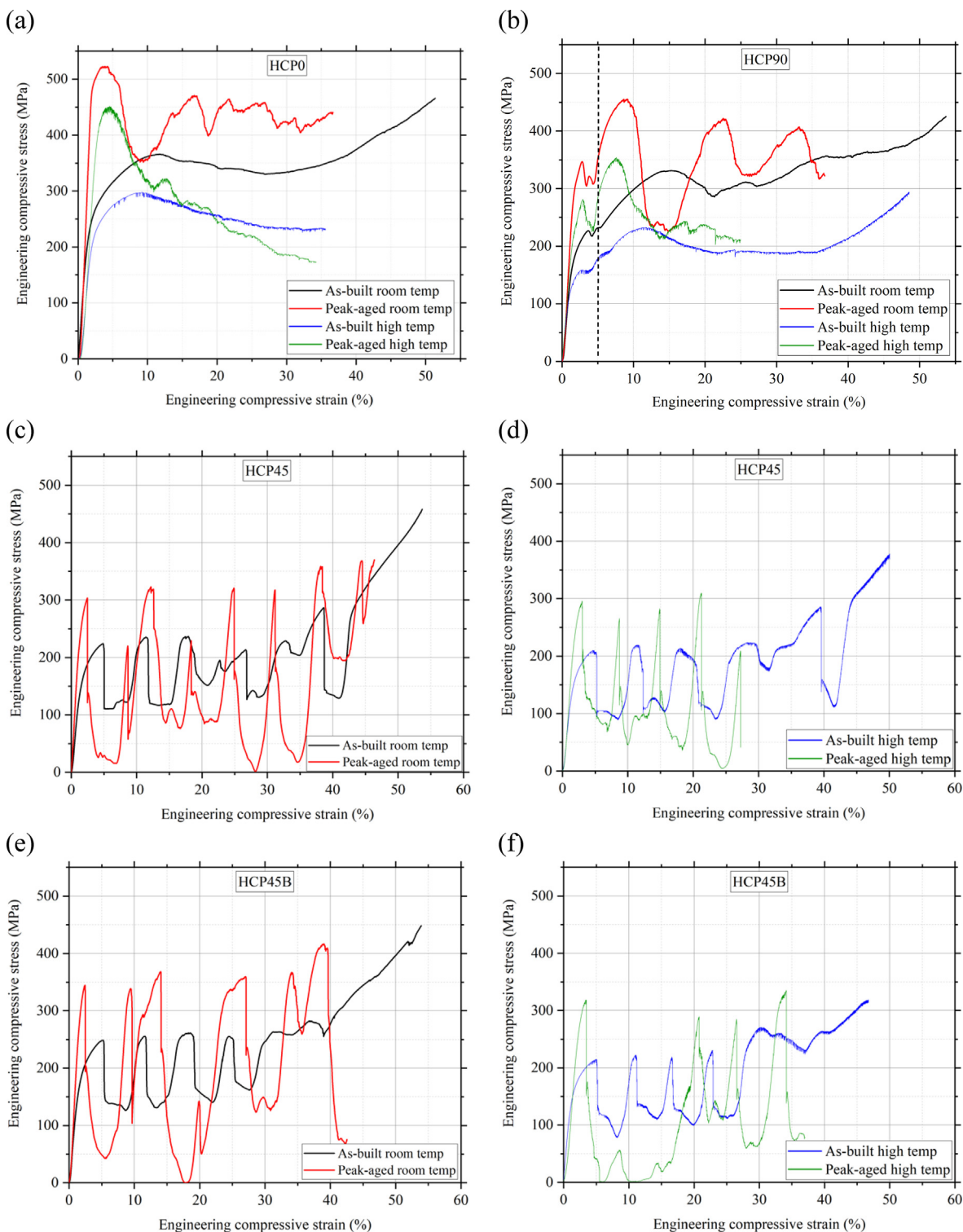
Fig. 11. Specific engineering compressive stress–strain curves corresponding to the as-built and peak-aged hexagonal Inconel 718 3D printed lattices tested at room and high (600 °C) temperatures: (a) HCP0, (b) HCP90, (c) HCP45, and (d) HCP45B.

representative room and high temperature engineering stress–strain curves corresponding to the single strut tensile specimens that were additively manufactured using the optimized set of LPBF processing parameters (Fig. 3). Table 4 summarizes the average yield stress, the ultimate tensile stress, and the tensile ductility corresponding to all the tests. The measured values lie within the

relatively wide property ranges published for LPBF-processed Inconel718, which are often better than those reported for the as-cast condition [29,30,35–39]. It can be seen that, for a given temperature, aging leads to a significant increase in the yield strength and in the ultimate tensile strength thanks to the precipitation hardening induced mainly by γ″ (Fig. 7b), and to a decrease

in ductility. Conversely, for a given microstructure, increasing the testing temperature results in softening and, in the peak-aged condition, in a moderate reduction in ductility (Table 4).

4.2. Coupled effect of microstructure and architecture on the mechanical behavior of additively manufactured Inconel718 superalloy lattices.

Our results show that microstructure, and in particular precipitates, influences the mechanical response of Inconel718 LPBF-processed lattice structures at the two studied temperatures in

several ways. Firstly, for all the architectures investigated, precipitation leads to significant increase in the yield strength of the lattice structures at room and high temperatures (Fig. 8, 11) and increasing the test temperature leads to a decrease in the lattice yield strength in both the as-built and peak-aged conditions. These variations of the strength of the lattice structures with precipitation and with the test temperature can be directly correlated to the variation of the strength of the base material described in Section 4.1.

Secondly, in the HCP45 and HCP45B lattices, which already exhibit a stretch-dominated response in the as-built condition,
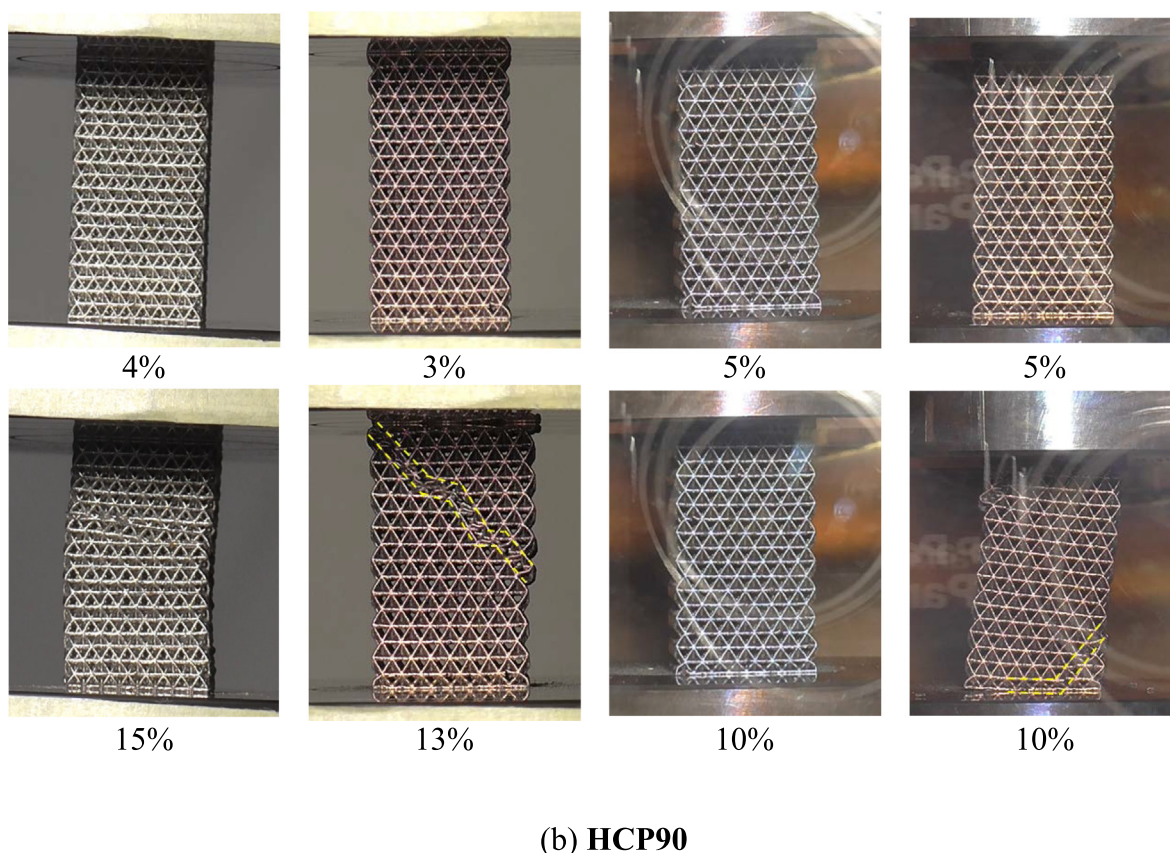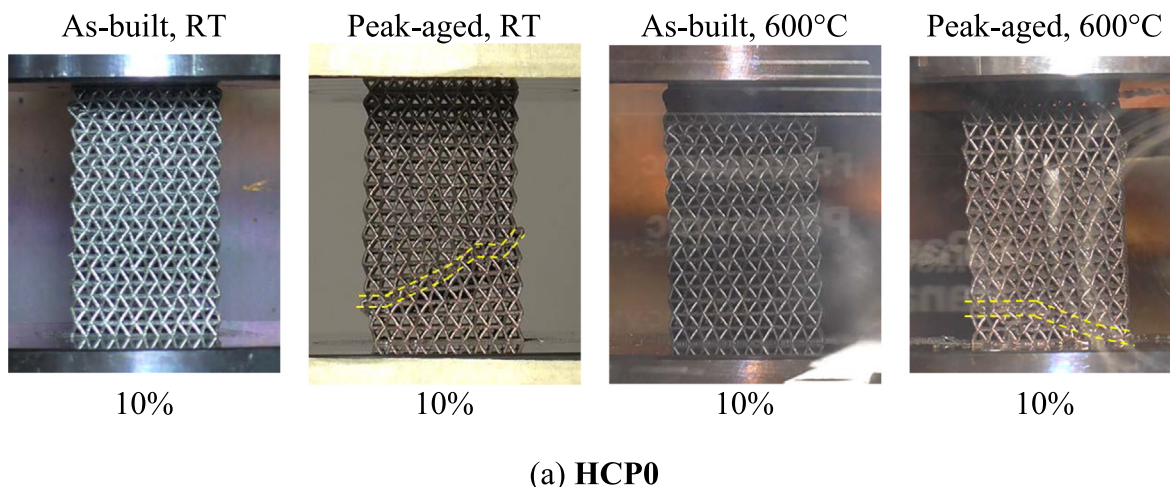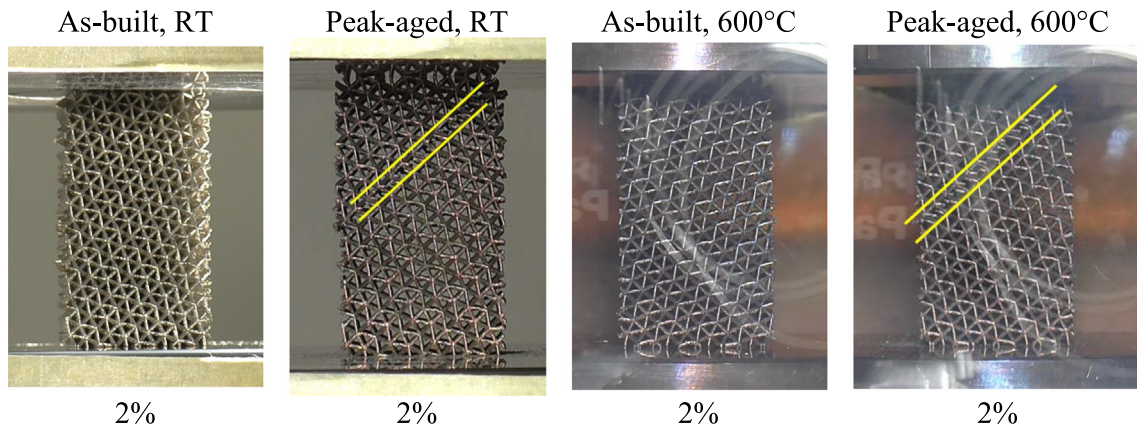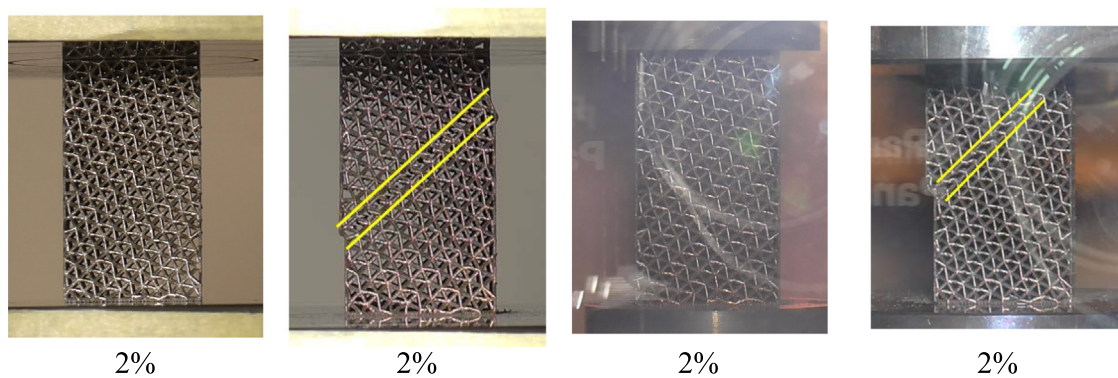

Fig. 12. Surfaces of the as-built and peak-aged (a) HCP0 and (b) HCP90 at different strain levels. The corresponding engineering strains are indicated below each image. The bands along which strut breakage was observed are highlighted in yellow. (For interpretation of the references to color in this figure legend, the reader is referred to the web version of this article.)

13

Fig. 13. Surfaces of the as-built and peak-aged (a) HCP45 and (b) HCP45B at different strain levels. The corresponding engineering strains are indicated below each image. The bands along which strut breakage was observed are highlighted in yellow. (For interpretation of the references to color in this figure legend, the reader is referred to the web version of this article.)
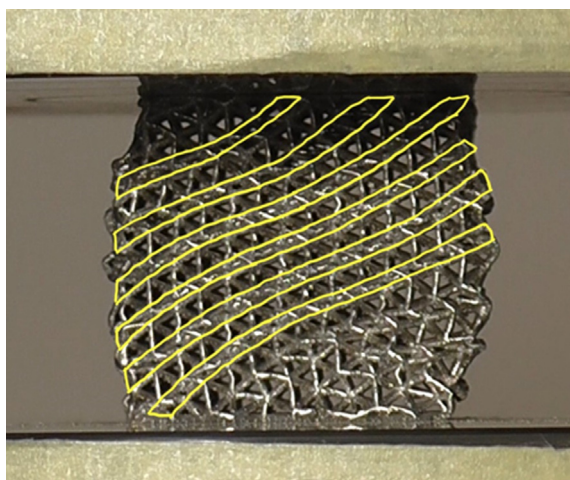

Fig. 14. Surface of an as-built HCP45B lattice deformed at room temperature to a strain of 30%. The bands formed with increasing deformation levels are highlighted in yellow.
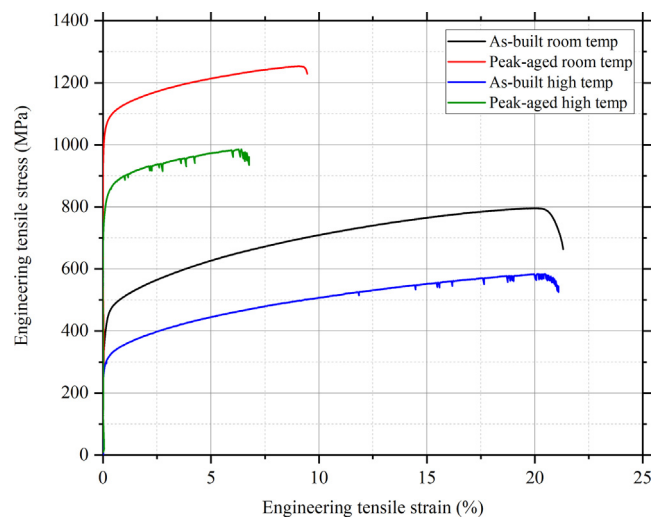
Fig. 15. Representative room and high (600 °C) temperature tensile stress–strain curves corresponding to the 3D printed Inconel 718 single-strut specimens in the as-built and peak aged conditions.

precipitation leads to a reduction of the width of the stress serrations and to more severe stress drops after the plastic yielding (Fig. 11). These two observations can be attributed to the decrease in the material ductility with precipitation (Fig. 15). Thirdly, in the peak-aged lattices, which exhibit a behavior similar to the stretch-dominated behavior irrespective of topology, the increase in the test temperature results in a reduction of the width of the stress serrations. This phenomenon can be ascribed to the reduction in strength and ductility with increasing temperature (Fig. 15), increasing the frequency of collapse and fracture of the peak-aged struts.

On the other hand, in the FCC, FCCXYZ, HCP0, and HCP90 lattices precipitation leads to a *transition* from bending-dominated to stretch-dominated behavior (Fig. 8, 9, 11, 12) and thus to a lar-

Table 4
Ductility, yield strength, and ultimate tensile strength values corresponding to the as-built and peak-aged single strut tensile samples, tested at room and high temperature.

Microstructure, Temperature	Ductility (%)	Yield strength (MPa)	Ultimate tensile strength (MPa)
As-built, RT	22.5 ± 1.5	490 ± 15	836 ± 17
Peak-aged, RT	12 ± 2	1044 ± 21	1243 ± 17
As-built, 600 °C	22.7 ± 1	321 ± 11	572 ± 8
Peak-aged, 600 °C	7 ± 2	873 ± 25	1028 ± 17

ger degree of strain localization (Fig. 9, 10, 12). It is believed that such transition may be attributed to a change in the strut deformation mode (from plastic hinging to elastic buckling) with aging. For example, in the case of FCσlattices, the yield strength is mainly governed by the deformation behaviour of [100] struts, whose slenderness ratio is larger than that of [110] struts. The elastic room temperature buckling stress (σ_{cr}) values may be calculated according to the Johnsoń s formula (Eq.1) (assuming the compressive stress was uniaxial and parallel to the [100] strut's axis):

$$\sigma_{cr,Johnson} = \sigma_y - \frac{1}{E}\left(\frac{\sigma_y}{2\pi}\right)^2 R^2 \tag{1}$$

where σ_y refers to the yield stress of the base material, R is the slenderness ratio ($R = L/r$, where L is the effective strut length and r is the radius of gyration) and E is the elastic modulus of the base material. It is worth noting that process defects (such porosity or surface roughness) can significantly lower the apparent elastic modulus and the yield stress of intricate lattice struts that were built with different angles with respect to the BD in comparison to vertically built dogbone strut samples for tensile tests. To reflect these effects on lattice struts, apparent values (instead of the true value) of the elastic modulus (72 GPa and 92 GPa) and yield stress (539 MPa and 1357 MPa) were used for the as-built and peak-aged conditions, respectively, for the FEA simulations (see Section 2.2). Taking into account that both ends of the struts are fixed, L is equal
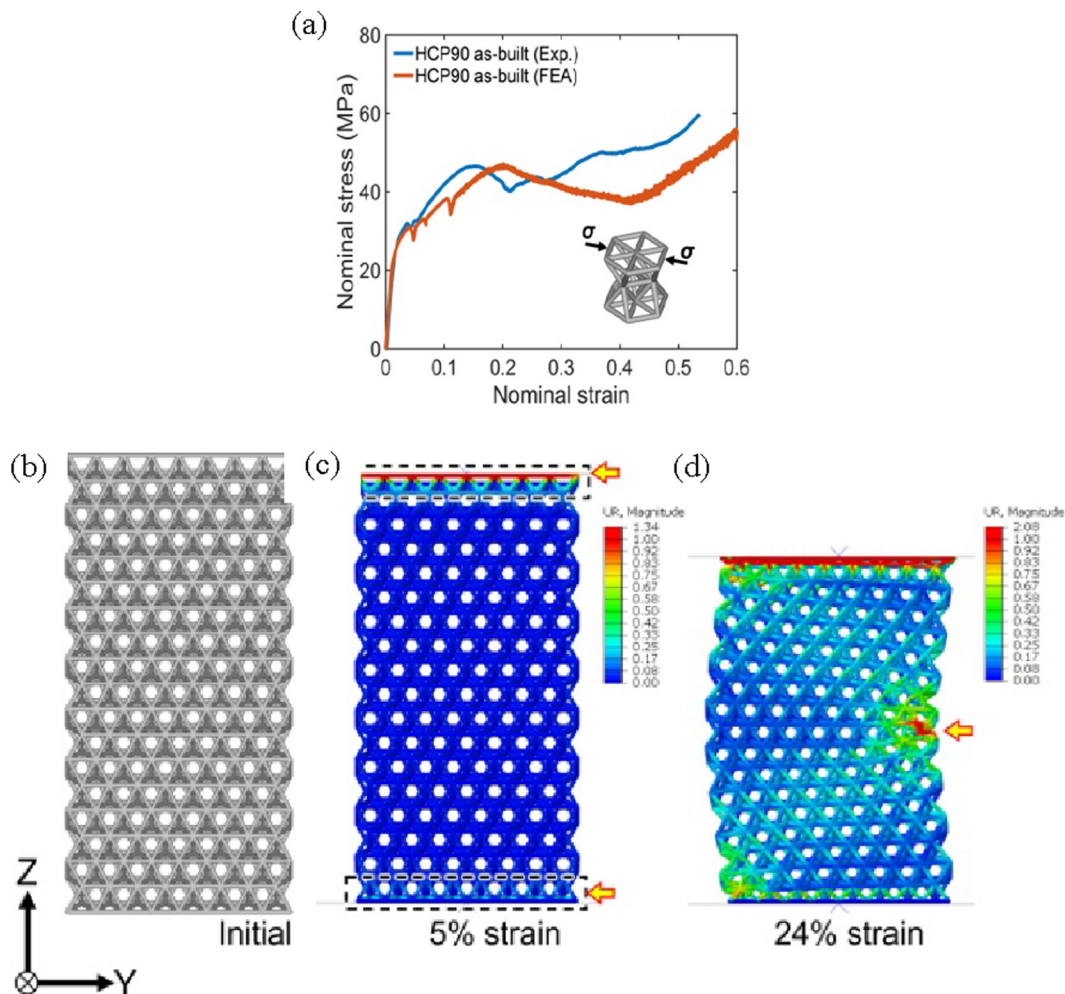

Fig. 16. (a) Comparison of the stress–strain behaviour between experiment and FE simulation of the HCP90 lattice in the as-built condition. (b-d) Deformation behaviour simulated by FEA: (b) un-deformed condition, (c) 5% nominal strain and (d) 24% nominal strain. Note: The field of notational displacement of element nodes is presented. Higher value indicates more severe deformation.

to half of the strut length (1.25 mm). Additionally, since $r = 0.1$, $R = 12.5$ and $\sigma_{cr, Johnson}$ is equal to 523 MPa and to 1278 MPa for the as-built and peak-aged conditions, respectively. The use of the Johnson's formula over the Euler formulation is justified based on the fact that R is smaller than the critical slenderness ratio (R_c), calculated using Eq. (2) below, which amounts, respectively, to 54 and 41 for the struts in the as-built and peak-aged conditions.

$$R_c = \sqrt{\frac{2\pi^2 E}{\sigma_y}} \qquad (2)$$

The calculated elastic buckling stress is relatively close to the yield stress for the as-built Inconel718 (539 MPa, Table 2) and significantly smaller than the yield stress for the peak-aged Inconel718 (1357 MPa, Table 2), indicating that the peak-aged lattices were more prone to elastic buckling while as-built lattice struts likely deformed by plastic hinges in consistent with the experimental observation. Additionally, the relatively large elongation of the as-built material at room temperature (22.5 %) allows more plastic deformation, thus leading to plastic hinges and would explain the stable post-yield deformation with rather smooth plastic flow stress response that is similar to the bending-dominated behavior. By contrast, given the elongation of the peak-aged Inconel718 (12 %) was much smaller than that of as-built part (Table 4 and Fig. 15), the peak-aged struts fractured at relatively small strains, resulting in abrupt loss of bearing ability and a stretching-dominated behaviour.

4.3. Origin of the low strain stress peak in the lattices with HCP90 topology.

As illustrated in Fig. 11, irrespective of microstructure and temperature, the HCP90 lattices exhibit a small stress serration at strains between 0.02 and 0.03. Fig. 12 proves that the origin of this serration cannot be attributed to the formation of a shear band as, at these low strains, homogeneous deformation still prevails. In order to elucidate the origin of the mentioned stress serration, FE modeling was carried out to determine the local stress and strain levels in the as-built HCP90 lattice with increasing compressive strain. Fig. 16a compares the HCP90 compression stress–strain curves obtained from experiments and simulation, showing that the simulation was able to reasonably capture the measured stress–strain behaviour. In particular, the first stress serration observed experimentally at a nominal strain smaller than 5 % was also predicted by the FE analysis. The simulation (Fig. 16c) shows that this serration is originated by the collapse of the struts at the very top and very bottom layers, which were much less supported compared to the struts inside the lattice. Once the struts were in contact with the compression plates, they were plastically deformed and collapsed right away. Subsequently, local densification led to the regain of stress levels. A few more similar serrations are observed at larger strains (Fig. 11b) until the initiation of the first shear band at about 15 % to 20 % (Fig. 16d) that caused a large reduction in stress. A considerable resemblance is found between Fig. 16d and the experimental results (Fig. 12b, left hand side column).

5. Conclusions

The aim of this work is to investigate the coupled effect of microstructure and topology on the mechanical behavior of Inconel718 lattices fabricated by LPBF. With that purpose, lattices with FCC, FCCXYZ, HCP0 (c-axis parallel to BD), HCP90 (c-axis at 90° to BD), HCP45 (c-axis at 45° to BD) and HCP45B (c-axis at 90° to BD and with borders) topologies were manufactured by LPBF and their mechanical behavior in the as-built and peak-aged condi-

tions was tested in compression at room and high temperature. The following conclusions can be drawn from the present study:

1. The microstructure of as-built lattices is a polycrystal formed by randomly oriented grains, slightly elongated along BD. The average grain length and width were, respectively, 16 ± 28 μm and 10 ± 14 μm. The grain boundary misorientation distribution resembled that of a random distribution of grains (MacKenzie), with an additional strong peak at misorientation angles lower than 5°, that is characteristic of LPBF-processed alloys. Grain interiors are populated by cells, and cell interiors are mostly a solid solution. Nb segregates to cell boundaries. Peak-aging of the lattices following LPBF processing gives rise to a precipitation, while the remaining microstructural features, including grain size, shape, and orientation, and grain boundary network, remained almost unchanged. Segregation of Mo and Ti to cell boundaries is observed following the heat treatment.

2. For all the topologies investigated, precipitation leads to significant strengthening of the lattice structures at room and high temperature; in turn, increasing the test temperature resulted in lattice softening in both the as-built and peak-aged conditions. These variations of the lattice strength with precipitation and with the test temperature can be directly correlated to the variation of the strength of the base material in similar microstructure and testing conditions, which is measured using dedicated printed specimens with gauge length with dimensions identical to those of single struts.

3. In the peak-aged lattices, which exhibit a stretch-dominated response irrespective of topology, increasing the test temperature results in a reduction in the width of the stress serrations. This can be ascribed to the decrease in strength and ductility of the peak-aged Inconel718 superalloy with increasing temperature.

4. In the FCC, FCCXYZ, HCP0, and HCP90 lattices, precipitation induced a transition from bending-dominated to stretch-dominated mechanical response. This may be attributed, in turn, to a transition in the dominant strut deformation mechanism, which is governed by plastic hinges in the as-built condition and by elastic buckling in the peak-aged condition.

5. This study proves the influential role of microstructure in the behaviour of additively manufactured metallic lattices and, as such, it highlights an exciting avenue of research focused on combining structure design and microstructure engineering.

Data availability

Data will be made available on request.

Declaration of Competing Interest

The authors declare that they have no known competing financial interests or personal relationships that could have appeared to influence the work reported in this paper.

Acknowledgments

cere thanks as well to Manuel Avella for his support with TEM examination. Javier García Molleja and Sergi Bafaluy are also acknowledged for their aid in tomography experiments and analysis.

Data availability

The raw/processed data required to reproduce these findings cannot be shared at this time due to technical or time limitations.

Appendix A. Supplementary material

Supplementary data to this article can be found online at https://doi.org/10.1016/j.matdes.2022.111294.

References

[1] T. Maconachie, M. Leary, B. Lozanovski, X. Zhang, M. Qian, O. Faruque, M. Brandt, SLM lattice structures: Properties, performance, applications and challenges, Mater. Des. 183 (2019) 108137.

[2] M. Benedetti, A. du Plessis, R.O. Ritchie, M. Dallago, S.M.J. Razavi, F. Berto, Architected cellular materials: A review on their mechanical properties towards fatigue-tolerant design and fabrication, Mater. Sci. Eng. R 144 (2021) 100606.

[3] L.Y. Chen, S.X. Liang, Y. Liu, L.C. Zhang, Additive manufacturing of metallic lattice structures: Unconstrained design, accurate fabrication, fascinated performances, and challenges, Mater. Sci. Eng. R 146 (2021) 100648.

[4] T. DebRoy, H.L. Wei, J.S. Zuback, T. Mukherjee, J.W. Elmer, J.O. Milewski, A.M. Beese, A. Wilson-Heid, A. De, W. Zhang, Additive manufacturing of metallic components – Process, structure and properties, Prog. Mater. Sci. 92 (2018) 112–224.

[5] D. Herzog, V. Seyda, E. Wycisk, C. Emmelmann, Additive manufacturing of metals, Acta Mater. 117 (2016) 371–392.

[6] Z. Alomar, F. Concli, A review of the selective laser melting lattice structures and their numerical models, Adv. Eng. Mater. 22 (12) (2020) 2000611.

[7] V.S. Deshpande, M.F. Ashby, N.A. Fleck, Foam topology: bending versus stretching dominated architectures, Acta Mater. 49 (2001) 1035.

[8] C. Liu, J. Lertthanasarn, M.S. Pham, The origin of the boundary strengthening in polycrystal-inspired architected materials, Nat. Comms. 12 (2021) 4600 (1-10).

[9] C. Pan, Y. Jan, J. Lu, Design and optimization of lattice structures: a review, Appl. Sci. 10 (2020) 6374.

[10] A.A. Zadpoor, Mechanical performance of additively manufactured meta-biomaterials, Acta Biomat. 85 (2019) 41.

[11] M. Leary, M. Mazur, H. Williams, E. Yang, A. Alghamdi, B. Lozanovski, X. Zhang, D. Shidid, L. Farahbod-Sternahl, G. Witt, I. Kelbassa, P. Choong, M. Qian, M. Brandt, Inconel 625 lattice structures manufactured by selective laser melting (SLM): Mechanical properties, deformation and failure modes, Mater. Des. 157 (2018) 179.

[12] T. Yu, H. Hyer, Y. Sohn, Y. Bai, D. Wu, Structure-property relationship in high strength and lightweight AlSi10Mg microlattices fabricated by selective laser melting, Mater. Des. 182 (2019) 108062.

[13] A. Takezawa, K. Yonekura, Y. Koizumi, X. Zhang, M. Kitamura, Isotropic Ti–6Al–4V lattice via topology optimization and electron-beam melting, Addit. Manuf. 22 (2018) 634.

[14] A. Moussa, D. Melancon, A. El Elmi, D. Pasini, Topology optimization of imperfect lattice materials built with process-induced defects via Powder Bed Fusion, Addit Manuf. 37 (2021) 101608.

[15] L. Bai, J. Zhang, Y. Xiong, X. Chen, Y. Sun, C. Gong, H. Pu, X. Wu, J. Luo, Influence of unit cell pose on the mechanical properties of Ti6Al4V lattice structures manufactured by selective laser melting, Addit. Manuf. 34 (2020) 101222.

[16] L. Zhang, B. Song, J.J. Fu, S.S. Wei, L. Yang, C.Z. Yan, H. Li, L. Gao, Y.S. Shi, Topology-optimized lattice structures with simultaneously high stiffness and light weight fabricated by selective laser melting: Design, manufacturing and characterization, J. Manuf. Process. 56 (2020) 1166–1177.

[17] Y. Liu, J. Zhang, X. Gu, Y. Zhou, Y. Yin, Q. Tan, M. Li, M.X. Zhang, Mechanical performance of a node reinforced body-centred cubic lattice structure manufactured via selective laser melting, Scr. Mater. 189 (2020) 95.

[18] M.S. Pham, C. Liu, I. Todd, J. Lertthanasarn, Damage-tolerant architected materials inspired by crystal microstructure, Nature 565 (2019) 305.

[19] E.D. Sanders, A. Pereira, G.H. Paulino, Optimal and continuous multilattice embedding, Sci. Adv. 7 (2021) 4838.

[20] J.C. Maxwell, On the calculation of the equilibrium and stiffness of frames, Lond. Edinburgh Dublin, Philos. Mag. J. Sci. 27 (1864) 294.

[21] M.F. Ashby, A.G. Evans, N.A. Fleck, L.J. Gibson, J.W. Hutchinson, H.N.G. Wadley, Metal Foams: A Design Guide, Butterworth-Heinemann, 2000.

[22] R. Wauthle, B. Vranckenc, B. Beynaerts, K. Jorissen, J. Schrooten, J.-P. Kruth, J. Van Humbeeck, Effects of build orientation and heat treatment on the microstructure and mechanical properties of selective laser melted Ti6Al4V lattice structures, Addit. Manuf. 5 (2015) 77–84.

[23] I. Maskery, N.T. Aboulkhair, A.O. Aremu, C.J. Tuck, I.A. Ashcroft, Compressive failure modes and energy absorption in additively manufactured double gyroid lattices, Addit. Manuf. 16 (2017) 24–29.

[24] P. Köhnen, C. Haase, J. Bültmanna, S. Ziegler, J.H. Schleifenbaum, W. Bleck, Mechanical properties and deformation behavior of additively manufactured lattice structures of stainless steel, Mater. Des. 145 (2018) 205–217.

[25] K. Hazeli, B.B. Babamiri, J. Indeck, A. Minor, H. Askari, Microstructure-topology relationship effects on the quasi-static and dynamic behavior of additively manufactured lattice structures, Mater. Des. 176 (2019) 107826.

[26] S. Banait, X. Jin, M. Campos, M.T. Pérez-Prado, Precipitation-induced transition in the mechanical behavior of 3D printed Inconel 718 bcc lattices, Scr. Mater. 203 (2021) 114075.

[27] D. Zhang, W. Niu, X. Cao, Z. Liu, Effect of standard heat treatment on the microstructure and mechanical properties of selective laser melting manufactured Inconel 718 superalloy, Mater. Sci. Eng. A 644 (2015) 32.

[28] M. Pröbstle, S. Neumeier, J. Hopfenmüller, L.P. Freund, T. Niendorf, D. Schwarze, M. Göken, Superior creep strength of a nickel-based superalloy produced by selective laser melting, Mater. Sci. Eng. A 674 (2016) 299.

[29] Inconel718 data sheet, Publication Number SMC-045, Spec. Met. Coorparation, 2007.

[30] C. Galera-Rueda, E. Nieto-Valeiras, M. Gardon, M.T. Pérez-Prado, J. LLorca, Effect of ZrH2 particles on the microstructure and mechanical properties of IN718 manufactured by selective laser melting, Mater. Sci. Eng. A 813 (2021) 141123.

[31] E. Hosseini, V.A. Popovich, A review of mechanical properties of additively manufactured Inconel 718, Addit. Manuf. 30 (2019) 100877.

[32] V. Vieira Reilli, A. Piglione, M.S. Pham, S. Primig, On the detailed morphological and chemical evolution of phases during laser powder bed fusion and common post-processing heat treatments of IN718, Addit. Manuf. 50 (2022) 102540.

[33] R. Reed, The Superalloys: Fundamentals and Applications, Cambridge University Press, Cambridge, UK, 2006.

[34] C.M. Cepeda-Jiménez, M. Castillo-Rodríguez, M.T. Pérez-Prado, Origin of the low precipitation hardening in magnesium alloys, Acta Mater. 165 (2019) 164.

[35] R. Schwab, V. Ruff, On the nature of the yield point phenomenon, Acta Mater. 61 (5) (2013) 1798–1808.

[36] Z. Wang, K. Guan, M. Gao, X. Li, X. Chen, X. Zeng, The microstructure and mechanical properties of deposited-IN718 by selective laser melting, J. Alloys Compd. 513 (2012) 518–523.

[37] A.T. Clare, R.S. Mishra, M. Merklein, H. Tan, I. Todd, L. Chechik, J. Li, M. Bambach, Alloy design and adaptation for additive manufacture, J. Mater. Proc. Tech. 199 (2022) 117358.

[38] M.J. Donachie, S.J. Donachie, Superalloys: A Technical Guide. ASM International, Materials Park, OH, USA, 2002.

[39] K.N. Amato, S.M. Gaytan, L.E. Murr, E. Martinez, P.W. Shindo, J. Hernandez, S. Collins, F. Medina, Microstructures and mechanical behavior of Inconel 718 fabricated by selective laser melting, Acta Mater. 60 (5) (2012) 2229–2239.